### **OPEN ACCESS**



# Flux Rope Merging and the Structure of Switchbacks in the Solar Wind

O. V. Agapitov<sup>1</sup>, J. F. Drake<sup>2,3</sup>, M. Swisdak<sup>3</sup>, S. D. Bale<sup>1</sup>, T. S. Horbury<sup>4</sup>, J. C. Kasper<sup>5,6</sup>, R. J. MacDowall<sup>7</sup>, F. S. Mozer<sup>1</sup>, T. D. Phan<sup>1</sup>, M. Pulupa<sup>1</sup>, N. E. Raouafi<sup>8</sup>, and M. Velli<sup>9</sup>, and M. Velli<sup>9</sup>, Page Sciences Laboratory, University of California Berkeley, Berkeley, CA, USA; agapitov@ssl.berkeley.edu

2 Department of Physics, the Institute for Physical Science and Technology and the Joint Space Institute, University of Maryland, MD, USA

3 Institute for Research in Electronics and Applied Physics, University of Maryland, College Park, MD, USA

4 The Blackett Laboratory, Imperial College London, London, UK

5 BWX Technologies, Inc., Washington DC, USA

6 Climate and Space Sciences and Engineering, University of Michigan, Ann Arbor, MI, USA

7 Code 695 NASA Goddard Space Flight Center, Greenbelt, MD, USA

8 Johns Hopkins Applied Physics Laboratory, Laurel, MD 20723, USA

9 Department of Earth, Planetary and Space Sciences, University of California, Los Angeles, CA, USA

Received 2021 August 23; revised 2021 November 22; accepted 2021 December 2; published 2022 February 7

#### Abstract

A major discovery of Parker Solar Probe (PSP) was the presence of large numbers of localized increases in the radial solar wind speed and associated sharp deflections of the magnetic field—switchbacks (SBs). A possible generation mechanism of SBs is through magnetic reconnection between open and closed magnetic flux near the solar surface, termed interchange reconnection, that leads to the ejection of flux ropes (FRs) into the solar wind. Observations also suggest that SBs undergo merging, consistent with an FR picture of these structures. The role of FR merging in controlling the structure of SBs in the solar wind is explored through direct observations, analytic analysis, and numerical simulations. Analytic analysis reveals key features of the structure of FRs and their scaling with heliocentric distance R, which are consistent with observations and demonstrate the critical role of merging in controlling the structure of SBs. FR merging is shown to energetically favor reductions in the strength of the wrapping magnetic field and the elongation of SBs. A further consequence is the resulting dominance of the axial magnetic field within SBs that leads to the observed characteristic sharp rotation of the magnetic field into the axial direction at the SB boundary. Finally, the radial scaling of the SB area in the FR model suggests that the observational probability of SB identification should be insensitive to R, which is consistent with the most recent statistical analysis of SB observations from PSP.

Unified Astronomy Thesaurus concepts: Heliosphere (711)

### 1. Introduction

A recent major discovery of Parker Solar Probe (PSP; Fox et al. 2016) was the presence of large numbers of localized velocity spikes associated with magnetic structures containing sudden deflections in the local radial magnetic field at 35.7-50  $R_{\odot}$  near the first PSP perihelion (Bale et al. 2019; Kasper et al. 2019 and others). The observed rotation angle inside these structures varies up to full reversal of the radial magnetic field component (Dudok de Wit et al. 2020), hence inspiring their designation as switchbacks (SBs). The time duration of an SB from the PSP data varies over a wide range of tens of seconds to tens of minutes (Dudok de Wit et al. 2020). Proton temperature enhancements are often associated with SBs (Agapitov et al. 2020; Krasnoselskikh et al. 2020; Woodham et al. 2021; Larosa et al. 2021). The plasma temperature increase inside SBs suggests that they may be magnetically isolated from the ambient solar wind. The constancy of the electron strahl pitch angle across the SB (Kasper et al. 2019) is an important constraint on SB generation mechanisms. Localized reversals of the magnetic field were observed in the coronal hole plasma of the Ulysses polar-crossing data set (e.g., Balogh et al. 1999; Yamauchi et al. 2004; Borovsky 2016; Neugebauer & Goldstein 2013), and were also seen in the

Original content from this work may be used under the terms of the Creative Commons Attribution 4.0 licence. Any further distribution of this work must maintain attribution to the author(s) and the title of the work, journal citation and DOI.

coronal hole plasma at 1 au (e.g., Kahler et al. 1996) and at 0.3 au (Horbury et al. 2018). However, PSP measurements from closer to the Sun (PSP's first perihelion was at 35.7  $R_{\odot}$  or 0.174 au, whereas Helios A and Helios B had perihelia at 0.31 and 0.29 au) have revealed that SBs undergo significant evolution as they propagate outward from the Sun from 30-50  $R_{\odot}$ —the distance covered by measurements in the first six encounters (the first three encounters had perihelia at 35.7  $R_{\odot}$ ). Compared to the SBs at perihelion, the SBs at 50  $R_{\odot}$  are more relaxed structures (Mozer et al. 2020): (1) the temperature of plasma inside the SB is reduced so that the difference with the ambient solar wind plasma temperature becomes insignificant; (2) the wave activity inside SBs and on their boundaries decreases by a factor of 5-10; (3) the rotation angle of the magnetic field direction inside SBs increases by a factor of 2; and (4) SB boundaries more closely resemble properties of more stable tangential discontinuities (Akhavan-Tafti et al. 2021). Thus, compared to the study by Horbury et al. (2018) in which there was little variation between SBs from Helios at 0.3 au, WIND at 1 au, and Ulysses at 2.4 au, it appears that SBs are evolving between 30 and 50  $R_{\odot}$ . The radial evolution is toward a reduction in the density and temperature jumps across SB boundaries.

Generation theories for SBs focus either on processes occurring deep in the solar atmosphere or in the expanding solar wind. One possibility is that SBs are produced locally through the amplification of turbulence in the expanding solar wind (Martinović et al. 2020; Tenerani et al. 2020; Shoda et al. 2021)

or shear-driven turbulence (Landi et al. 2006; Ruffolo et al. 2020; Schwadron & McComas 2021). However, a key observation—the sharp rise in the ion temperature at the boundaries of the SB (Farrell et al. 2020; Mozer et al. 2020; Larosa et al. 2021) may be inconsistent with a model based on the amplification of Alfvénic turbulence.

Coronal sources (Dudok de Wit et al. 2020; Krasnoselskikh et al. 2020; Macneil et al. 2020; Woodham et al. 2021) that include reconnection between open and closed magnetic flux (interchange reconnection) (Fisk & Kasper 2020; Zank et al. 2020; Drake et al. 2021) or reconnection associated with jets (Dudok de Wit et al. 2020; He et al. 2020; Sterling & Moore 2020) can produce magnetic flux ropes (FRs) and inject them into the solar wind. Small-scale magnetic FRs in the solar wind at 1 au were reported by Moldwin et al. (2000) from the International Monitoring Platform (IMP-8) and the WIND spacecraft observations. Magnetic reconnection as the source for FRs in the Earth magnetosphere (magnetic flux transfer events at the Earth's magnetopause) has been previously discussed (Russell & Elphic 1978; Lee & Fu 1985; Slavin et al. 2003). It has been suggested that FRs in the Earth's magnetosheath (flux transfer events) resulted from the ripping off of flux tubes from the neartail dayside magnetopause through magnetic reconnection based on International Sun-Earth Explorers ISEE 1 and ISEE 2 (Russell & Elphic 1978; Lee & Fu 1985) and GEOTAIL (Slavin et al. 2003) observations. The structures were observed to be force-free FRs without significant velocity enhancement and with comparable perturbation of all magnetic field components and similar radial and transverse spatial scales. The statistical properties of FR structures in the solar wind were reported by Chen et al. (2020, 2021) based on events recorded during PSP's first approach to the Sun. Drake et al. (2021) used two-dimensional particle-in-cell (PIC) simulations to study the hypothesis that SBs are FR structures that are ejected into the solar wind by bursty interchange reconnection. It was found that FRs with radial-field deflection (up to full reversal), nearly constant B magnitude, and temperature enhancements are naturally generated by interchange reconnection; and FR initial conditions relax into structures that match PSP observations reasonably well (Drake et al. 2021). The possible connection between SBs and FRs was discussed by Chen & Hu (2022). Chen et al. (2021) showed that FRs can be embedded within SBs.

The open question is the physical processes transforming FRs produced during interchange reconnection deep in the corona into the FRs that characterize SBs. Compared with FRs expected from interchange reconnection, SBs have axial magnetic fields that are strong compared with the magnetic field that wraps the axial field, are highly elongated along the direction of the ambient solar wind magnetic field, and are characterized by flows with high Alfvénicity. A process that can play a key role in the evolution of SBs is magnetic reconnection on the boundaries (Phan et al. 2020). Features found at the boundaries of several SBs (Froment et al. 2021) indicate that reconnection with the ambient solar wind field can play a role in the erosive decay of SBs. However, observations of SBs in the entire range of heliocentric distances from 20  $R_{\odot}$ to 2.4 au suggest that reconnection with the solar wind magnetic field is suppressed, presumably due either to the velocity shear (Chen et al. 1997; Dahlburg et al. 1997) or diamagnetic stabilization (Phan et al. 2010, 2013; Swisdak et al. 2010). In addition to reconnection with the ambient solar wind magnetic field, FRs injected into the solar

wind via interchange reconnection can also undergo merger (Drake et al. 2021). The FR (magnetic island) coalescence process has been studied by numerical simulations (Odstrcil et al. 2003; Oka et al. 2010; Pritchett 2008; Zhou et al. 2014), by remote spacecraft measurements of electrons accelerated during merging process (Song et al. 2012), direct measurements during crossing of a series of merging FRs of coronal mass ejection in the solar wind, and by in situ measurements by the four Magnetosphere MultiScale (MMS) spacecraft at the terrestrial magnetopause (Zhou et al. 2017). Drake et al. (2006), Pritchett (2008), Oka et al. (2010), Song et al. (2012), and Zhou et al. (2014) find that merging is very dynamic and releases large amounts of energy. The comprehensive numerical study of FR coalescence in guide field reconnection by Zhou et al. (2014) showed that the coalescence of macroscopic FRs can provide significant energy dissipation and can be an efficient mechanism for particle energization. FR merging was active in the numerical model of SB formation presented by Drake et al. (2021), where a train of FRs merged through reconnection.

In this paper we explore the structure of FRs sourced from interchange reconnection in the solar corona as they propagate outward in the solar wind, including the scaling of their crosssectional area (in the plane transverse to the SB axis—often this plane is close to the R-N plane in heliospheric coordinates, which is used to present the cross-sectional plane in the following for simplicity of notation), their aspect ratio (R versus N direction), their interaction during propagation, the energetics of merging, and its consequences for evolution of the FR structure. We demonstrate that the outward expansion of FRs in the solar wind combined with FR merging causes FRs generated during interchange reconnection to transition to FRs that match the character of SBs. To perform this study we present theoretical arguments, the results of PIC simulations based on the further development of the model presented by Drake et al. (2021) and PSP observations.

### 2. SB Characteristics from PSP Measurements

We use measurements from PSP of electric and magnetic fields made by the PSP FIELDS suite of instruments (Bale et al. 2016). The vector magnetic field is measured from DC to several tens of hertz by the fluxgate magnetometer, while magnetic fluctuations above 10 Hz are measured by the Search-Coil Magnetometer (Jannet et al. 2021). The DC electric measurements are made by the EFI electric antennas. All these data products are provided by the Digital Fields Board (Malaspina et al. 2016). The sampling rate of the waveforms corresponds to the survey cadence during the early part of the solar encounter phase. During the close encounter phase this cadence increases fourfold. The proton velocity, density, and temperature are provided by the SWEAP suite (Kasper et al. 2016). The Solar Probe Cup (SPC) Faraday cups (Case et al. 2020) provide moments of the reduced distribution function of ions: density, velocity, and radial component of the thermal velocity. Their cadence is 0.22 s. Finally, we consider the electron pitch angle distribution from the Solar Probe ANalyzer-Electron (Whittlesey et al. 2020), whose cadence is 28 s.

A typical SB is a perturbation of the solar wind structure containing a proton bulk velocity spike and an associated localized deflection of the magnetic field direction. The magnetic field structure of an SB recorded at about  $36~R_{\odot}$  from the Sun (2018 November 5—the first PSP perihelion) is

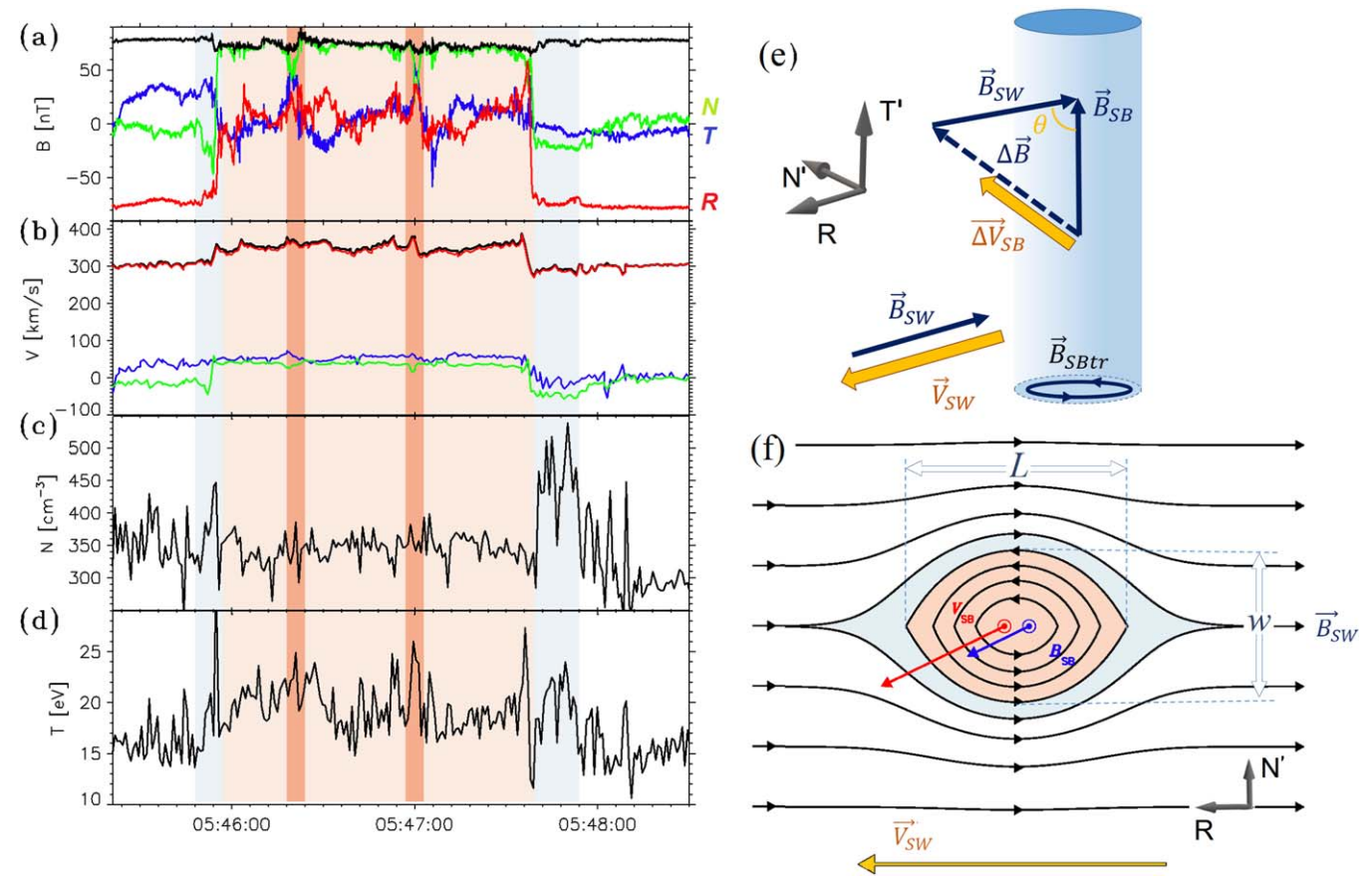


Figure 1. An SB recorded by PSP at  $35.7 R_{\odot}$  on 2018 November 4 during the first perihelion: (a) the magnetic field components (in the RTN system: with the red, blue, and green curves corresponding to R,T,N components). The radial component of the magnetic field exhibits an almost complete rotation inside the SB and becomes positive (anti-sunward). The magnitude is shown by the black curve; (b) the proton bulk velocity components (in the RTN system with the same color scheme as in panel (a)) and the absolute value of the bulk velocity (the black curve); (c) the proton density and (d) the parallel proton temperature. (e) an FR (SB) schematic with the parameters discussed in the text. (f) SB structure in the R-N' plane transverse to the SB axis (usually close to the R-N plane of the RTN system). The color scheme matches that in panels (a)–(d) where the boundary region is colored light blue and the core region is light red.

shown in Figure 1(a) (the components are shown in the RTN coordinate system with R the radial direction directed from the Sun center, N the normal to the ecliptic plane component, and T the azimuthal component). The sharp rotation of the direction of the magnetic field at the boundary while remaining nearly constant in magnitude, and the radial magnetic field changing sign, are typical characteristics of these events. The boundaries range in widths from tens of kilometers (several proton inertial lengths) to tens of thousands of kilometers (Krasnoselskikh et al. 2020; Larosa et al. 2021; Mozer et al. 2020). The perturbation of the proton bulk velocity (Figure 1(b)) follows the magnetic field perturbation illustrating the Alfvénicity of SBs, i.e.,  $\Delta \mathbf{\textit{B}}_{\rm SB} \sim \Delta V_{\rm SB}$ . The plasma density enhancements (highlighted in light blue in Figure 1(c)) are typical for SB boundaries ( $\sim 30\%$  on average (Farrell et al. 2020)). The enhancement of the parallel proton thermal velocity inside the SB to  $63 \pm 3 \text{ km s}^{-1}$  (with the ambient value of  $55 \pm 3 \text{ km s}^{-1}$ ) is shown in Figure 1(d). SBs often have a complex internal structure highlighted in dark red in Figure 1—the structure of this particular SB has been resolved making use of the Grad-Shafranov reconstruction by Chen & Hu (2022) and showed that this SB consists of three FRs, confirming the presumption for this event by Drake et al. (2021).

A characteristic parameter for SBs is the angle that the axial magnetic field makes with respect to the direction of solar wind magnetic field ( $\theta$  in the schematic in Figure 1(e)). SBs move in the

solar wind frame with a velocity approximately proportional to  $\Delta B_{\rm SB}$ —the Alfvénicity condition (Kasper et al. 2019). While the dominant magnetic field component inside an SB is typically axial (often close to the T direction), SBs also have transverse components, schematically shown in Figure 1(f) (Krasnoselskikh et al. 2020; Drake et al. 2021; Larosa et al. 2021). These properties of SBs have been well reproduced in numerical simulations of FRs in the solar wind (Drake et al. 2021).

# 3. Analytic Analysis of the Radial Scaling of FRs, Their Aspect Ratio and the Energetics of Merging

A key goal required to establish FRs as possible sources of SBs is to understand the physics basis for their structure that yields observational predictions. Such predictions include the scaling of the size of SBs with radial distance from the Sun, their aspect ratio, and their internal magnetic structure, including the large ratio of the axial magnetic field to that defined by the plane of the ambient solar wind. In the following, for simplicity we take the solar wind magnetic field to be radial  $B_{\rm SW} = B_R$ , the axial SB magnetic field  $B_{\rm SB}$  to be in the RTN T direction (in a general case the SB coordinate system RT'N' differs from the RTN system with the T'-axis directed along the averaged  $B_{\rm SB}$ , i.e., the SB axis, and the common R-axis with the RTN system. However, the following discussion is valid for cases where the angle between  $B_{\rm SB}$  and

 $B_{\rm SW}$  is in the range of  $\pi/2 \pm \pi/6$ , which is satisfied for more than 80% of SBs observed by PSP) and the width w of the SB or FR to be in the N direction. (The transverse magnetic field components inside the SB are  $B_r$  and  $B_N$ , and since  $|B_R| \approx |B_T|$ ,  $|B_r|$  and  $|B_N|$  are much smaller than  $|B_R|$  and  $|B_T|$ .) This coordinate systems can, of course, be generalized so that the ambient solar wind magnetic field lies along the direction of the Parker spiral. We also note that the axial magnetic field might have a component along the radial direction but for simplicity neglect that in the discussion that follows. In the following we presume that SBs are FRs and explore the consequences of this model to understand SB structure.

A key characteristic of FRs concerns the scaling of their area A with radial heliocentric distance R. This scaling follows from the conservation of the total axial magnetic flux under the assumption that magnetic reconnection with the ambient solar wind magnetic field is not active. Such an assumption is likely to break down sufficiently far from the Sun and is perhaps the reason that SBs are less probable in 1 au observations than closer to the Sun. The axial SB magnetic field  $B_{SB} = B_T$ nominally scales as  $R^{-1}$  due to the expansion of the solar wind in the N direction. However, such a scaling with radius is inconsistent with the balance of magnetic pressure within a FR with that of the ambient solar wind radial field  $B_R$ , which scales as  $R^{-2}$ . Thus, pressure balance requires that the FR area A increase to reduce  $B_T$  to match the local  $B_R$ . Flux conservation then yields  $B_T A \sim B_R A \sim R^{-2} A$  so that A scales as  $R^2$ . In invoking pressure balance we have neglected the magnetic field  $B_r$  and  $B_N$ , the radial and normal magnetic fields of the FR, in comparison with  $B_T$ . This assumption is consistent with most observations. The scaling of A with  $R^2$  yields no information on the scaling of the characteristic width w (along N) and length L(along R) of the FR other than  $A \sim \pi wL$ .

Observations reveal that the aspect ratio L/w of the SBs is large (Horbury et al. 2020; Laker et al. 2021; Mozer et al. 2021). Thus, a fundamental question is what physics leads to such large aspect ratios? We suggest that it is the weakness of the magnetic field which wraps the FR,  $B_r$  and  $B_N$ , compared with  $B_R$  and  $B_T$ , which allows the FR to be squashed by the strong solar wind magnetic field. The axial field  $B_T$  prevents the compression of the FR but provides no restoring force to prevent the FR from being squashed to a state in which  $B_r/B_N \sim L/w \gg 1$ . Note that the magnetic flux  $\psi$  that wraps the FR is given by  $\psi \sim B_N L \sim B_r w$ . As the solar wind magnetic field squashes the FR, the tension force in the R direction within the FR scales like

$$F_R \sim \frac{1}{4\pi} B_N \frac{\partial B_r}{\partial N} \sim \frac{1}{4\pi} B_N \frac{B_r}{w}.$$
 (1)

The schematic in Figure 1(f) illustrates the forces involved. This tension force must be balanced by a corresponding tension force  $F_N$ . In a round FR the balance between these two forces cause the FR to be round. However, the force  $F_N \sim \left(\frac{B_r}{4\pi L}\right)B_N$  within the FR is negligible for  $L\gg w$  and the restoring force must arise from the weak bending of the solar wind magnetic field due to its distortion by the FR. Within the solar wind a weak magnetic field  $B_N \sim w B_R/L$  produces the restoring force that limits compression of the FR,

$$F_N \sim \frac{1}{4\pi} B_R \frac{1}{L} \frac{w}{L} B_R. \tag{2}$$

The balance between the two tension forces yields the relation,

$$B_N B_r \sim (w^2/L^2) B_R^2$$
. (3)

As the FR aspect ratio changes,  $B_N$ ,  $B_r$ , w, and L change, so an expression for w has to be evaluated at a fixed A and  $\psi$ , which are invariant as the aspect ratio changes. The resulting expression for w is

$$\frac{w^4}{A^2} \sim \frac{\psi^2}{\pi A B_P^2}.\tag{4}$$

It is convenient to rewrite this relation in terms of more obvious physical parameters as

$$\pi w^2/A \sim B_r^2/B_R^2. \tag{5}$$

This equation reveals that it is the weak magnetic field  $B_r$  that wraps the FR that allows the FR to be compressed to produce the highly elongated SBs seen in the data. Thus, a fundamental question is why  $B_r$  is reduced compared with  $B_R$  as FRs propagate outward in the solar wind. It is not a consequence of the simple radial expansion of the solar wind.  $B_r$  within the FR has the same scaling properties as  $B_R$  since the FR expands in both the T and N directions.

Here we suggest that while FRs that result from interchange reconnection near the solar surface generally have an aspect ratio of order unity, they undergo mergers as they propagate outward in the solar wind and that the merging process reduces the magnetic field  $B_r$  below that of the ambient  $B_R$ . Indeed, it is the reduction of  $B_r$  and the associated magnetic energy that facilitates FR merger. The merger of two FRs of similar magnetic flux yields a final FR with increased area A and with a constrained magnetic flux (Fermo et al. 2010). These relations are unchanged when the FR is elongated. However, the final FR aspect ratio and the change in  $B_r$  is impacted by the elongation of the FRs. Equation (1) reveals that the FR width w increases by the factor  $2^{1/4}$  when the merger of two FRs of equal area and flux merge, which results from the doubling in the area. Since the flux is conserved,  $B_r$  is reduced by the factor  $(1/2)^{1/4}$ . Since  $B_r$  dominates  $B_N$ , the magnetic energy decreases during merger with the energy going to heating the plasma within and around the FR, as has been shown in observations of the coalescence of macroscopic FRs (Drake et al. 2006; Zhou et al. 2014, 2017). Thus, the merger of squashed FRs is energetically favorable and leads to the reduction of the magnetic field that wraps the magnetic flux and increased elongation of FRs.

This result suggests that FRs should be increasingly elongated with radial distance from the Sun. Further, the reduction of  $B_r$  and also  $B_N$  within the FR means that the axial magnetic field of FRs dominates that of the other components. This explains one of the key features of SBs observations, the sharp rotation of the magnetic field in the solar wind into the axial direction upon entry into an SB.

# 4. Dynamics of the Process of SBs Merging: The Numerical Results

Drake et al. (2021) presented a model of SB generation by interchange reconnection between open and closed flux in the low corona that created FRs that ejected them with high velocity outward in the solar wind. The structures have a strong axial magnetic field wrapped by magnetic flux and exhibit the

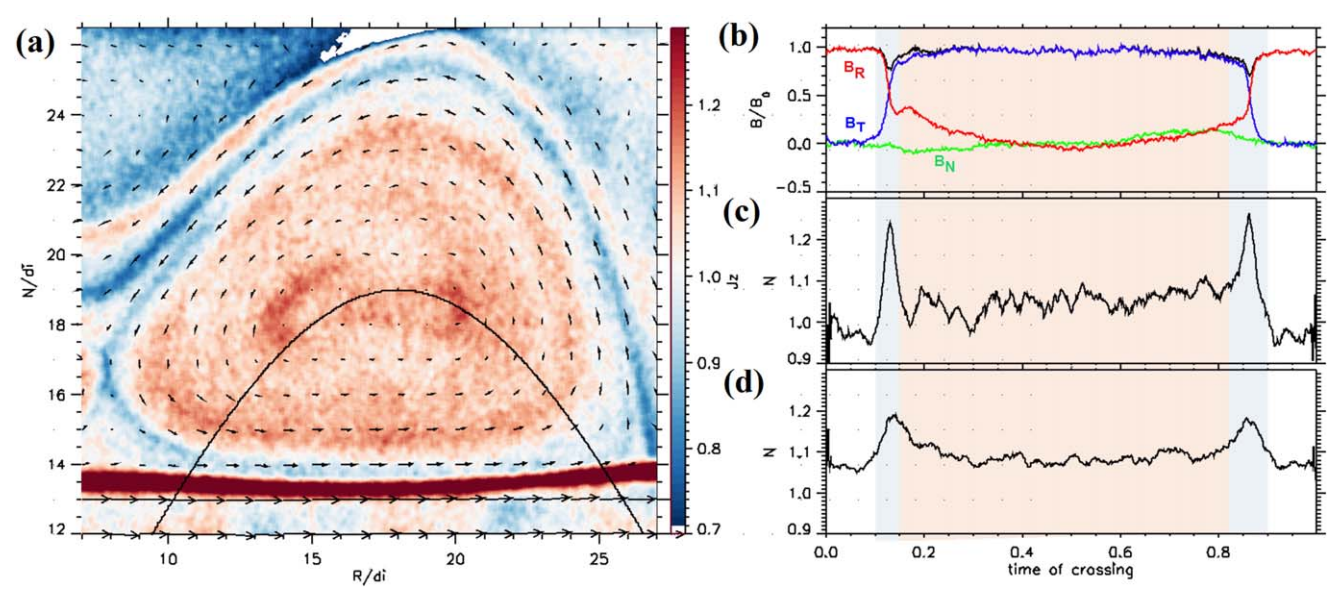


**Figure 2.** The SB structure from the PIC simulation ( $\Omega_i t = 270$ ) in the R-N plane (similar cut as in the schematic in Figure 1(f). (a) the transverse magnetic field (arrows) and the axial current  $J_T$ ; (b) the structure of the magnetic field (the  $B_R$ ,  $B_T$ , and  $B_N$  components are shown by the red, green, and blue curves, respectively); (c) and (d) the plasma density and temperature. The cuts are along the N direction through the center of the FR.

characteristic internal rotation of the radial magnetic field. The dynamics of this system reproduced well the magnetic structure of SBs seen in PSP data and also indicated the tendency of FRs to merge. We focus here on the details of this merging process to identify the observational features and the consequences for SB structure. Interchange reconnection favors the production of a series of FRs that have similar axial magnetic fields. We perform numerical simulations with the PIC code p3d (Zeiler et al. 2002) using a setup similar to that presented in Drake et al. (2021). The initial field configuration consists of a straight background magnetic field  $B_0$  directed along the R-axis (we adapt the numerical system coordinates to the RTN system in the solar wind), a weak initial reversed magnetic field ( $\sim$ 0.2  $B_0$ ), and the guide field  $B_T$  in the region where the initial radial field reverses to be of order  $B_R$ , so, that the total magnetic field magnitude is a constant across the region of reversed flux. The initial plasma density and temperature are uniform. The simulation results are presented in normalized units: magnetic field to  $B_0$ , time to  $\Omega_i^{-1}$  and distance to the ion inertial length  $d_i$ . The computational domain is given by  $L_x \times L_y = 40.96d_i \times 40.96d_i$  with the grid spacing given by  $\delta x = \delta y = 0.05 d_i$ , and 100 particles per cell. The reversed magnetic field, which drives reconnection and eventually produces the magnetic field  $B_R$  and  $B_N$  that wraps the FR, is weak compared with  $B_T$  as in SB observations from PSP data.

Reconnection started from noise leads to generation of many FRs, which then merge. The magnetic field structure transverse to the SB axis is shown in Figure 2(a) superimposed over the axial electron current. It reveals the characteristic magnetic island structure with wrapped magnetic field components,  $B_R$  and  $B_N$ . Shown in Figure 2 are the magnetic field components (in panel (b)), the density (in panel (c)), and the temperature (in panel (d)). The magnetic field configuration and the plasma parameters are in a good agreement with the SB structure obtained from PSP measurements: sharp rotation of the magnetic field direction at the SB boundaries, almost constant magnetic field magnitude and plasma density inside with localized magnetic dips (Agapitov et al. 2020;

Farrell et al. 2020), and density enhancements at the boundaries (Farrell et al. 2020; Larosa et al. 2021).

The time series of three merging FRs (from left to right, FR1, FR2, and FR3) from the simulation is shown in Figure 3. First, FR2 and FR3 merge into a single larger structure FR2-3 with lower internal transverse magnetic field. Later, at  $\Omega_i t = 225$ , FR1 approaches FR2-3 and at around  $\Omega_i t = 270$  merging of FR1 and FR2-3 starts.

The reconnection regions (zoomed images of boxes #1 and #2 from Figure 3) shown in Figure 4 present the details of the magnetic field and velocity structure during the merging of the FRs. A current sheet (CS) develops between the merging islands. It is predominantly in the N-T plane and has a width about the proton inertial length in both cases in Figure 4. Across the CS  $B_N$  changes sign. The inflow velocity  $V_{\text{inflow}}$ normal to the reconnection CS plane (the blue curves) reveals that plasma flows toward the reconnecting CS with velocity about 0.5 of the Alfvén velocity based on the reconnecting magnetic field magnitude ( $V_{Ar}$ ) in the second case (Figures 4(d) -(f)). The plasma outflow is directed mostly along the N-axis with velocity about 0.8-0.9  $V_{Ar}$ . In the first case (Figures 4(a)– (c)) the inflow and outflow velocities are similar but the motion of the right FR provides an additional velocity  $\sim 0.5~V_{\rm Ar}$  that leads to an increase of the negative values to about  $V_{Ar}$ . The first case (Figures 4(a)–(c)) does not show a significant outflow so that there is no change of in the sign of the correlation of  $B_{\text{recon}}$  and  $V_{\text{outflow}}$  during the CS crossing.

## 5. PSP Observations of SB Structure

The features of merged FRs seen in the simulations, including localized current layers and localized density and temperature enhancements, are often seen in the SB structures observed in the solar wind by PSP. An important question is therefore whether there is evidence for merging in the observational data. An example is presented in Figure 5 showing two SBs (highlighted in red in Figure 5) approaching each other and driving a density enhancement between them (highlighted in blue). The second SB has a complex inner

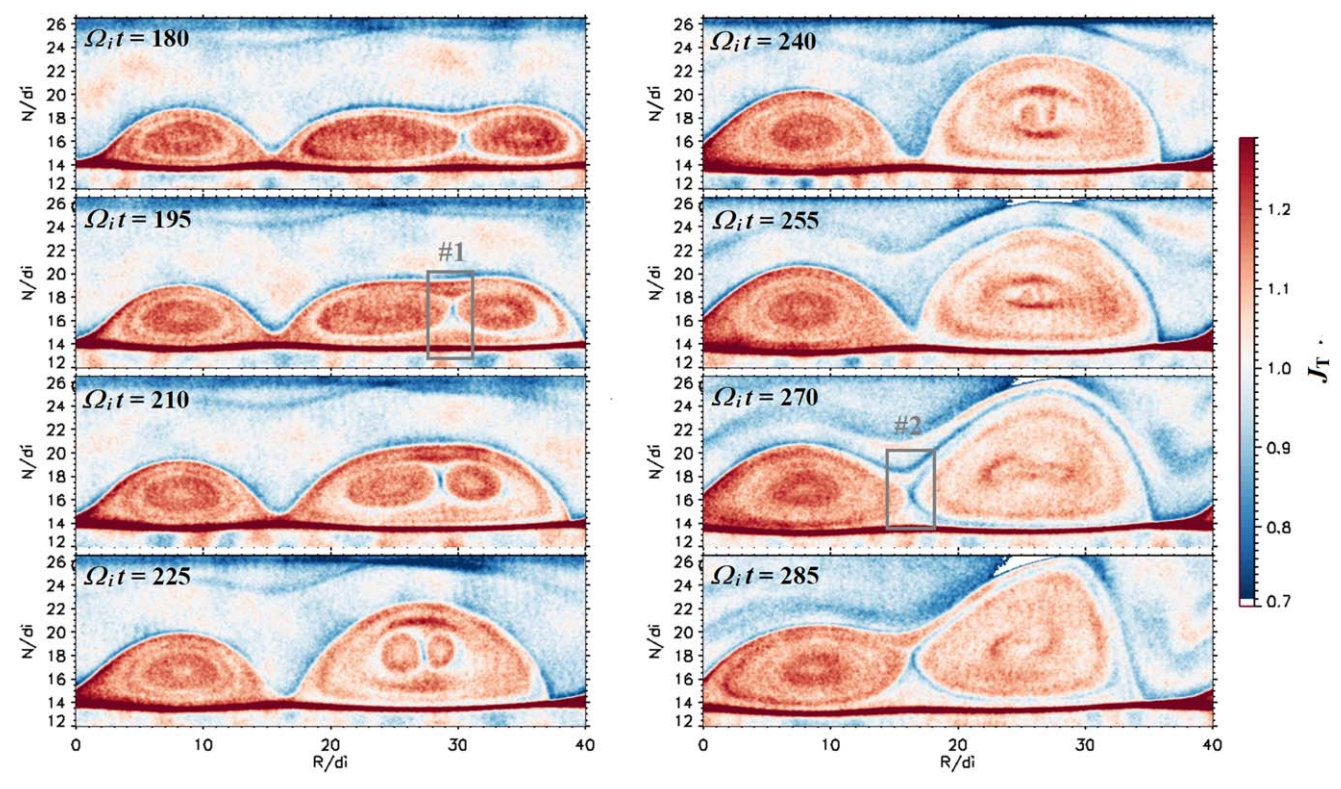


**Figure 3.** Dynamics of the FRs merging shown in the out-of-plane current  $J_T$  in the R-N plane.

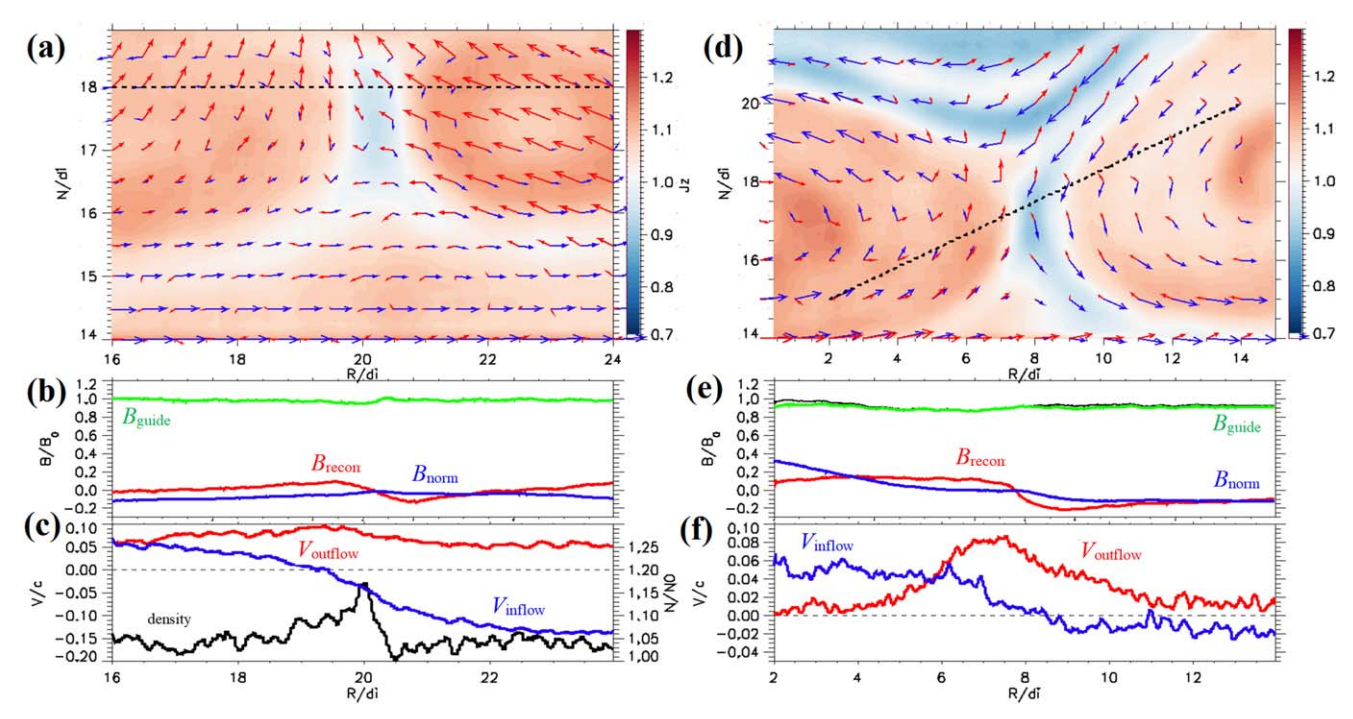


**Figure 4.** Reconnection regions (marked in Figure 3 with the gray boxes) during the merging of FR2 and FR3 (in panels (a)–(c)) and FR2-3 and FR1 (panels (d)–(f)). Panel (a) shows the out-of-plane electron current  $J_{eT}$ , and the structure of the magnetic field (blue arrows) and plasma flow (red arrows) in the reconnection region #1 (FR2 and FR3 merging). The data along the black dashed line are shown in panels (b) and (c): in panel (b) the components of magnetic field in the CS coordinate system (the guide field is green, the normal component is blue, and the reconnecting component is red); and in panel (c) the in-plane components of plasma flow velocity (the blue curve is the inflow velocity—the normal component to the CS; the red curve is the outflow velocity) with the plasma density shown by the black curve with the scale in the right. The right panels (d)–(f) show the merger of FR1 and FR2-3.

structure of magnetic field and plasma velocity perturbations: it consists of four regions with three transition regions—CSs marked by deep red. Based on the structure of FRs from the

simulation we suggest that the second SB consists of four or five FRs. This scenario is supported by the structure of the plasma density and temperature, which have sharp, localized

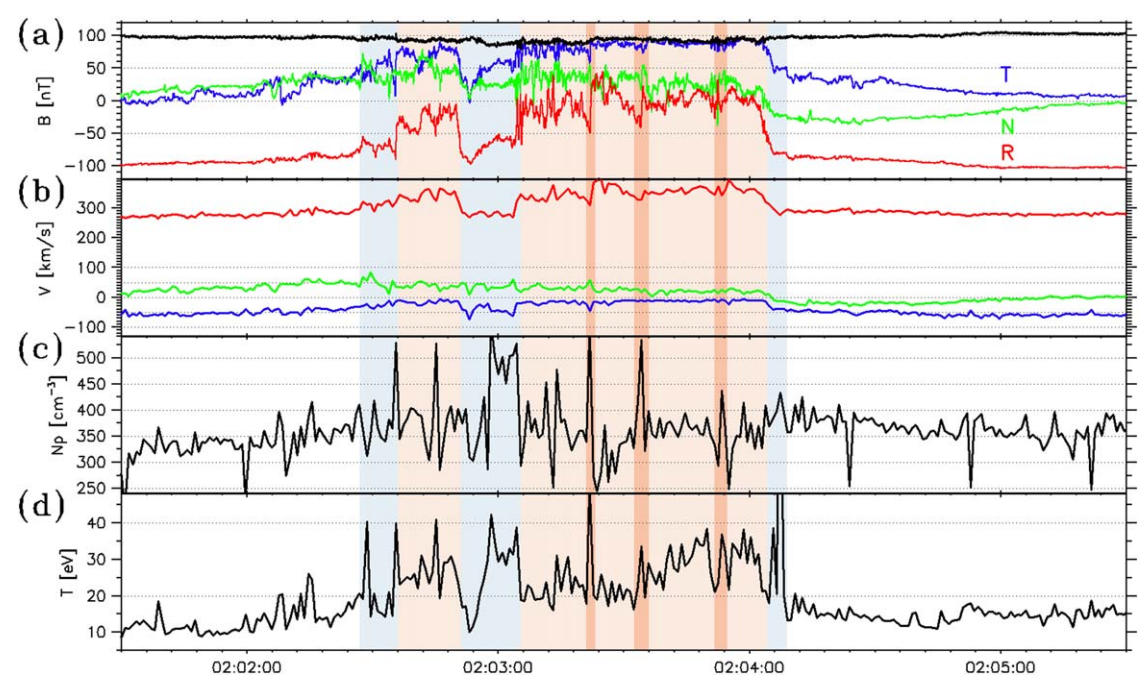


**Figure 5.** Two SBs (highlighted in light red) recorded on 2018 November 6 by PSP. The panels from top to bottom present the magnetic field in the RTN coordinate system (a) and the proton bulk velocity (b); the proton density (c) and the parallel proton temperature (d). The deep red regions highlight the boundaries between distinct regions of the second SB.

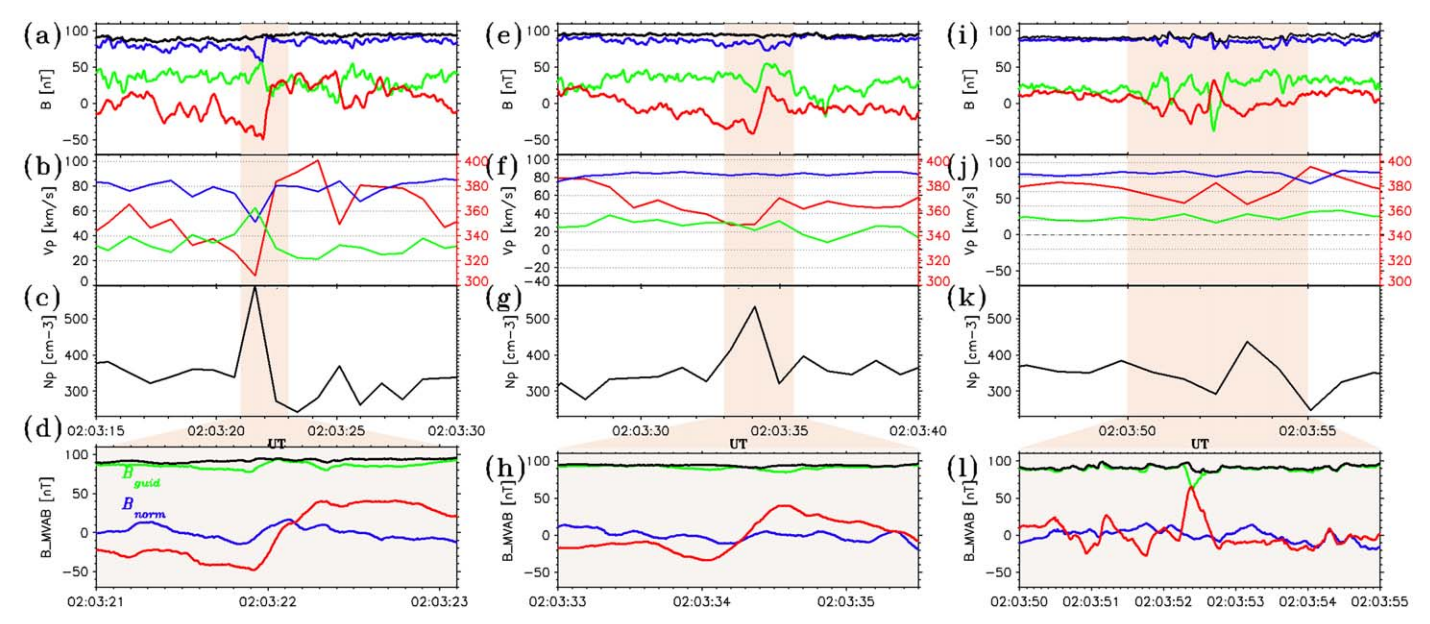


**Figure 6.** Zoomed intervals highlighted in Figure 5. CS#1 (a) the magnetic field components and magnitude; (b) plasma bulk velocity components; (c) proton density; (d) the magnetic field component in the CS frame (the interval highlighted in panel (b)). The second and third intervals (CS#2 and CS#3) highlighted in Figure 5 are presented in panels (e)–(h) and (i)–(l), respectively.

enhancements around the CSs. The structure of the three CSs (highlighted in red in Figure 5) is shown in three expanded views in Figure 6.

The first interval (CS#1: 2:03:15–2:03:30) reveals signatures that would seem to suggest that merging of two FRs recently terminated. The transverse to the FR axis magnetic field (red) reverses sign across a well-defined current layer that produces a magnetic field jump of  $\pm (50 \pm 5)$  nT. The guide field (blue) is  $90 \pm 5$  nT, i.e.,  $\sim 2$  times greater than the maximal value of the transverse field. The CS thickness is  $12 \pm 3$  km (the proton inertial length is  $12 \pm 1$  km). The

structure of the magnetic field for CS#1 is similar to that of the reconnecting CS between the two merging FRs from the simulation in Figures 4(a)–(c). However, the velocities for this interval shown in Figure 6(b) do not reveal the characteristic Alfvénic reconnection outflow centered on the current layer, which persists even in the case of reconnection with a strong guide field (Gosling & Phan 2013; Drake et al. 2021; Phan et al. 2020). Rather, the flows exhibit the typical Alfvénic relation between velocity and magnetic that has been documented in earlier PSP data (Kasper et al. 2019; Phan et al. 2020). Thus, in spite of the intense current layer seen in

this interval, the velocity data does not support the idea that reconnection is ongoing. Nevertheless, the presence of strong current layers and other signatures that are normally attributed to active reconnection requires explanation.

A limitation of the reconnection and merging simulations presented in Section 4 was the absence of the characteristic Alfvénic flows present in the solar wind. These Alfvénic flows might prevent FR merging since it is known that sheared flows across a current layer can prevent reconnection (Cowley & Owen 1989; Chen et al. 1997). We have initiated a simulation study of FR merger that includes parallel flows with  $V = \alpha V_A$  b in the initial condition. The parameter is a  $\alpha$  constant that typically ranges between 0 and 1, the latter corresponding to fully Alfvénic flows. During periods in the solar wind when flows are Alfvénic in character, the parameter  $\alpha$  is typically of order unity or less. To study FR merger, we initialize the system with two equal-sized, cylindrical FRs with a strong ambient guide field that has a magnitude that is twice the peak in-plane magnetic field. The initial FR equilibrium is the same as that reported previously (Drake et al. 2021). The two FRs are overlapped slightly to initiate reconnection. Here we show an example from one of the simulations to illustrate the qualitative behavior of FR merger and its relation to the PSP observations. Further details will be presented in a more complete paper (Drake et al. 2021). Simulation data for the parameter  $\alpha = 0.75$ is shown in Figure 7. Panels (a), (b) and (c), (d) illustrate the out-of-plane current with overlying magnetic field lines at two times. In panel (a) reconnection is well developed and a strong current layer has developed between the two FRs. At this time strong outflows from the magnetic x-line have developed as shown in panel (b). The outflows are nearly centered on the current layer as expected in a traditional reconnection outflow. Note the downflow on the right side of the FR and the upflow on the left that correspond to plasma circulation within each of the FRs. At late time in (c) and (d) magnetic reconnection and FR merging has ended. Nevertheless, a strong current layer remains: the cut along the black line in panel (c) reveals the reversal of  $B_y$  with almost constant  $B_x$  and  $B_z$  (the guide field) in panel (e); the reversal of  $B_y$  with the corresponding component of plasma flow velocity in panel (f) indicate evidence that along a cut across the current layer, the direction of the vertical flow reverses along with the reversal in the corresponding vertical magnetic field (as seen in the observations in Figures 6(a), (b) and (e), (f)) and as is required to maintain the Alfvénicity of the flows); the enhancement of plasma density and proton temperature in the current layer are shown in panel (g) and are also consistent with observations (Figure 7(g)). At this time the FRs begin to rotate around each other with the FR on the right moving up and the FR on the left moving down. This is evident from the displacement of the FRs in panel (c) as well as the flows in panel (d). Thus, the late time structure of the magnetic field and flows are qualitatively consistent with the observational data in Figure 6.

The saturation of the FR merging is a consequence of energy transfer from the released magnetic energy into the plasma flow circulating on the reconnecting field line. As the reconnected field line shortens, the parallel streaming velocity increases, increasing the Alfvénicity inside the FRs because of the invariance of the action  $V_{||}$  L, with L the field line length. When the Alfvénicity approaches unity, reconnection is energetically unfavorable. This has important implications for understanding the measured Alfvénicity in the PSP observations

(Drake et al. 2021). The increase in the Alfvénicity as a consequence of the merging suggests the possible connection of the Alfvénicity with the proton temperature inside the FRs since merger increases both the Alfvénicity and the plasma temperature. The variation in several plasma parameters inside the different FRs is displayed in Figure 8: the magnetic fields B and  $B_T$  (Figure 8(a)), the radial magnetic field  $B_R$  (Figure 8(b)), the Alfvénicity (Figure 8(c)), and plasma temperature (Figure 8(d)). The FRs are separated by the CS and the FRs with higher proton temperature inside have higher levels of Alfvénicity (Figure 8(e)). This suggests that the increase in both parameters is likely the result of merging but that merging has now ended, leaving the remnant current layers separating distinct FRs as shown in Figure 7.

The second CS (2:03:33–2:03:40, CS#2) presents a crossing of the CS with a magnetic field change of  $\pm(35\pm5)$  nT (the guide field of  $90\pm5$  nT is similar to CS#1) and the velocity following the changes of the reconnecting magnetic field. The current layer thickness is  $16\pm5$  km (the proton inertial length is  $12\pm1$  km) with a similar density enhancement as in CS#1. The third interval (2:03:47–2:03:57, CS#3) does not reveal a strong CS and reversed magnetic field. The peak in the density suggests that this boundary could correspond to a post-merging configuration. Thus, CSs#1–3 are possibly examples of the CS resulting from merging of FRs in the solar wind and conserved in time due to increased (in the process of merging) Alfvénicity.

Due to significant elongation along the radial direction SBs most probably merge along their long dimension—the CS in CSs#1-3 have normals directed predominantly along *N*-axis (the schematic of the system geometry is shown in Figure 9).

The structure of perturbations suggest that the large SB in Figure 5 is the result of the partial merging of four (or five) FRs with similar parameters (magnetic field magnitude and direction, plasma density) that probably originated from the same source.

# 6. Discussion and Conclusions

Drake et al. (2021) showed that FRs can form in the low corona through interchange reconnection and can be injected into the solar wind. FRs in reconnecting CSs are generated at small spatial scales as the CS narrows and reconnection develops (Biskamp 1986; Drake et al. 2006; Bhattacharjee et al. 2009; Cassak et al. 2009). We have shown here that:

- While FRs that result from interchange reconnection near the solar surface are generally likely to form with an aspect ratio of order unity and comparable axial and transverse magnetic field, they undergo geometrical changes while propagating outward in the solar wind, tending to significant elongation along the background magnetic field, and interact with each other through merging.
- 2. Merging occurs through the slow reconnection of the weak magnetic field that wraps the stronger axial magnetic field, and thus, reduces the strength of the wrapping magnetic field and heats the plasma inside the structure. Merging of FRs is energetically favorable and increases the axial plasma flow speed leading to increased Alfvénicity of the structure.
- 3. When the Alfvénicity approaches unity  $(\Delta \mathbf{\textit{B}}_{SB}/(4\pi m_p)^{1/2} \approx \Delta \textit{\textit{V}}_{SB})$  merging becomes energetically unfavorable, and

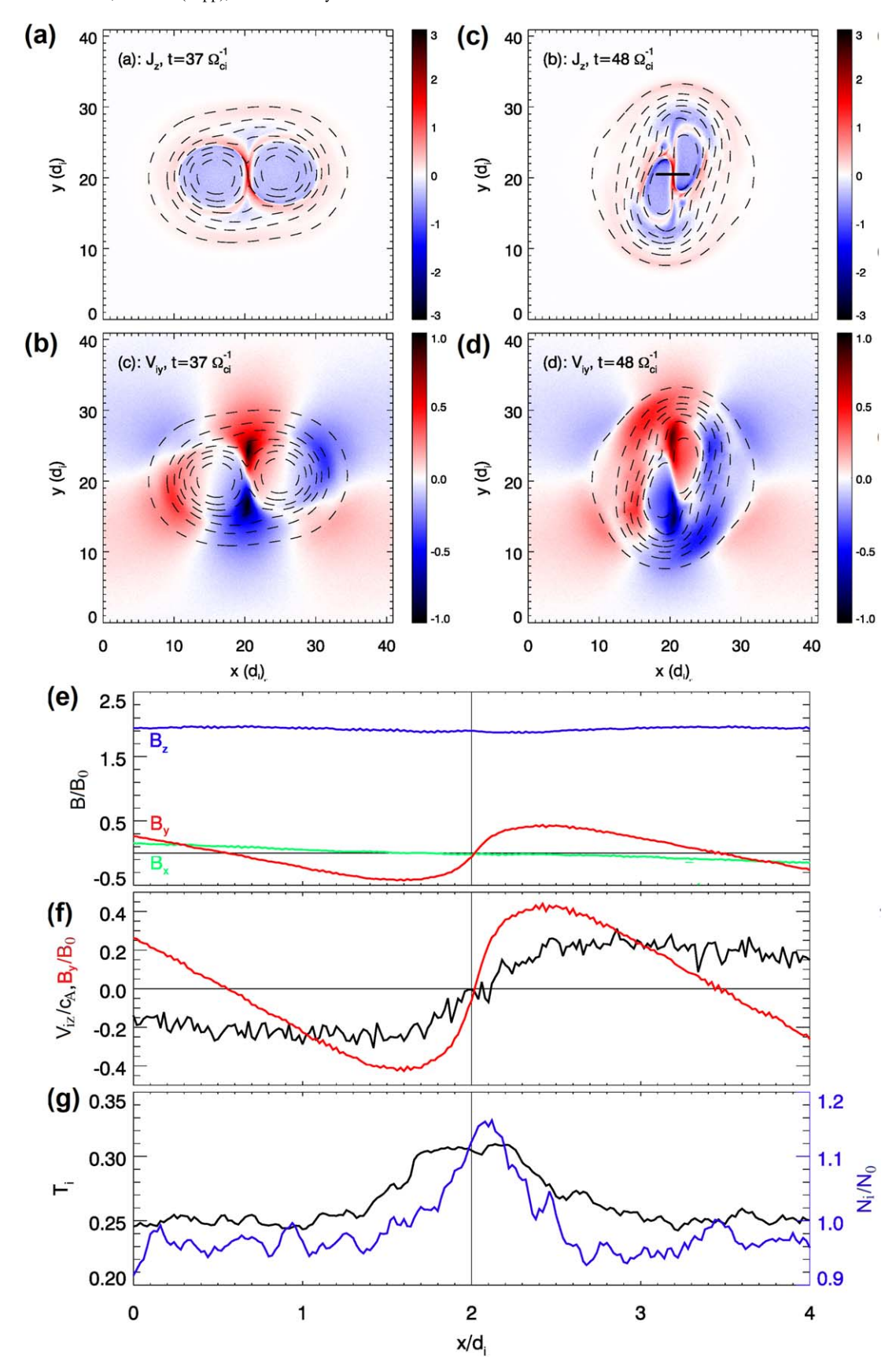


**Figure 7.** Results of a simulation of FR merger with initial Alfvénic flow. Out-of-plane current and magnetic field lines during merging in (a) and after merging ends in (c). Vertical flows  $V_y$  in (b) and (d) corresponding to the times in (a) and (c). The data along the black line in panel (c) is shown in panels (e)–(g): (e) the magnetic field; (f) the reversing magnetic field component ( $B_y$ , the red curve) and the corresponding component of the plasma flow velocity ( $V_y$ , the blue curve); (g) the plasma density (the blue curve) and temperature (the black curve).

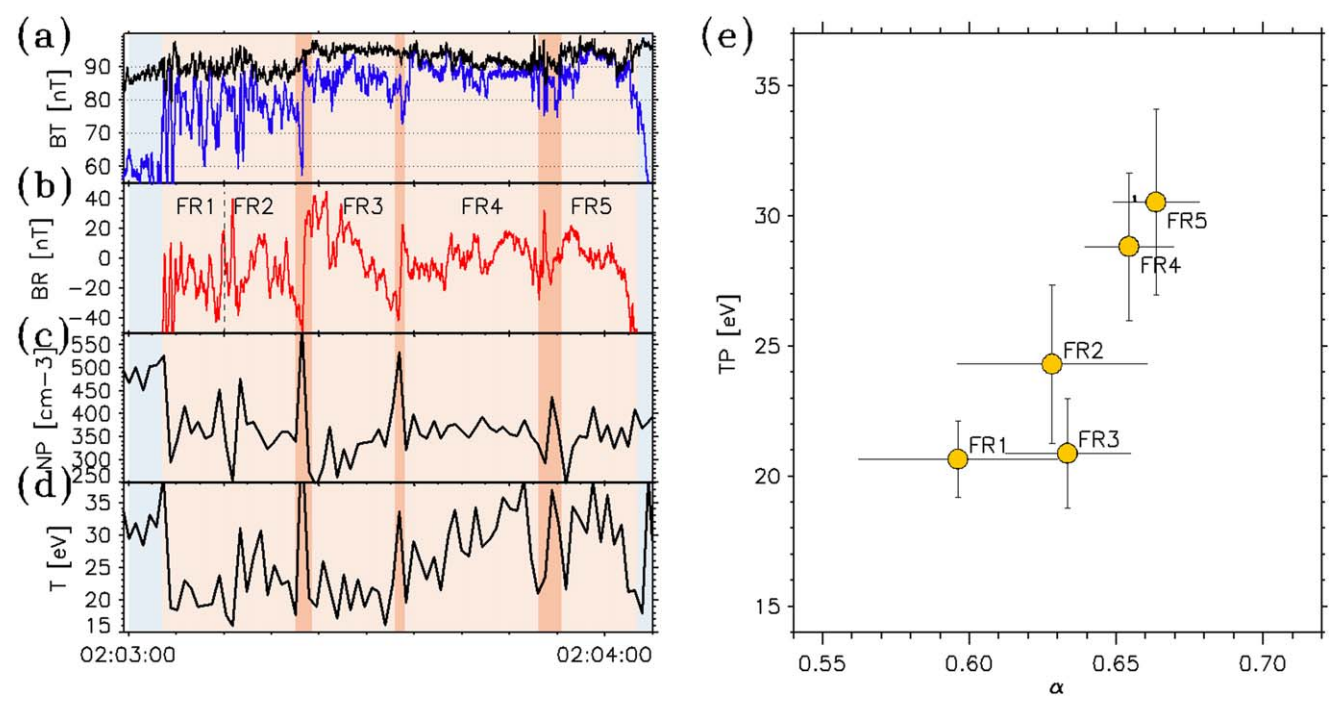
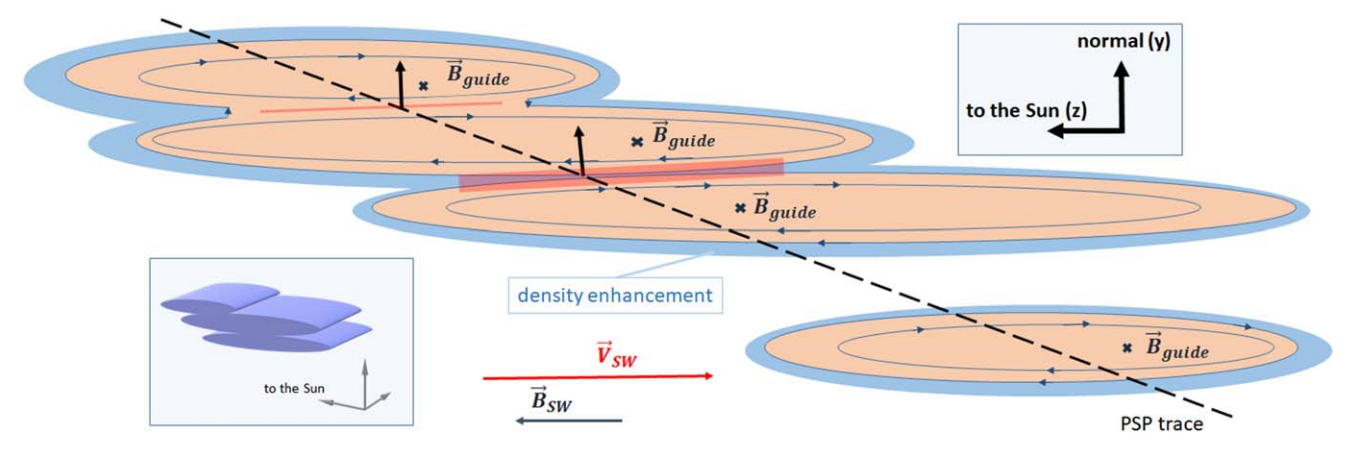


Figure 8. Structure of the SB from Figure 5: (a) the T component of magnetic field (the blue curve); (b) the radial component of magnetic field (the R component) indicating the magnetic island structure of the SB components; (c) the Alfvénicity  $\alpha$  inside the SB; (d) the radial temperature inside the SB; (e) the dependence of the proton temperature on the Alfvénicity for the structure components (individual FRs) composing the SB.



**Figure 9.** Schematic of the structure of SBs from Figure 5 in the R-N plane. The scales are arbitrary. The red arrows show the outflow at the edges of the reconnection CS. The black arrows show the direction of a normal to the CS at the point of crossing by the spacecraft.

thus the saturation of FR merging is a consequence of energy transfer from the reconnected magnetic field into the plasma flow and thermal energy. When the FR Alfvénicity becomes significant FR merger saturates before it is complete, which leads to a remnant CS with magnetic and velocity characteristics consistent with PSP observations. Thus, the multi-FR structure with the conserved in time remnant current sheaths that characterizes many solar winds is a consequence of incomplete FR merger.

- 4. This has important implications for understanding the measured Alfvénicity in the PSP observations. The strength of the wrapping magnetic field (decreasing through FR merging) controls the elongation of FRs: a weaker wrapping magnetic field allows the ambient solar wind magnetic field to squash and elongate the FRs (and therefore SBs). Thus, SBs become
- increasingly elongated along the solar wind magnetic field with radial distance from the Sun. The result is that the SBs evolve to a state with a weak magnetic field that wraps the SB compared to it is axial field. Therefore, a sharp rotation of the magnetic field is observed at SB boundaries.
- 5. The reduction of the magnetic field that wraps the FR during merging might be responsible for the observed plasma temperature enhancement inside SBs. Thus, the signature of FRs mergers can be the relation of plasma temperature and Alfvénicity level inside an SB since both increase during merging. The signatures of SB merging similar to those obtained in the numerical modeling are often seen in PSP observations of SBs at 20–50  $R_{\odot}$ . This suggests that merging of FRs is a significant part of the evolution of SBs from the FRs generated in the low corona to the magnetic structures observed by PSP.

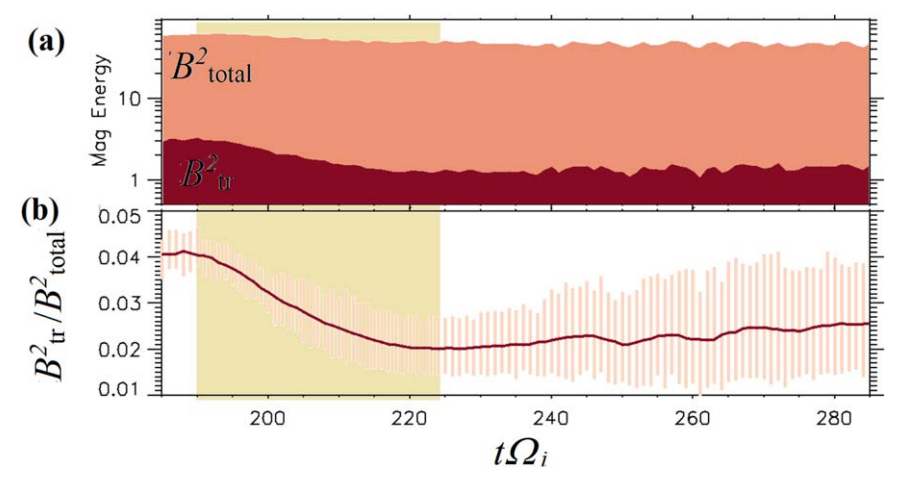


**Figure A1.** Dynamics of the merger of FRs FR2 and FR3. Magnetic energy (panel (a) the total energy is marked with light red and the transverse energy is marked with dark red) and (b) the contribution from the transversal (wrapped) magnetic field (averaged over the entire FR cross-section area) in FR2-3 from Figure 3. The error bars represent the values averaged over different crossings of FB2-3 by a virtual spacecraft. The interval of FB2 and FB3 merging is highlighted in yellow.

O.V.A., J.F.D., and M.S. were supported by NASA grants 80NNSC19K0848 and 80NSSC22K0417. O.V.A. was partially supported by NSF grant 1914670 and NASA grants 80NSSC20K0218, 80NSSC22K0417, 80NSSC20K0697, and 80NSSC21K1770.

# **Appendix**

Magnetic energy versus time during the merger of FRs FR2 and FR3 is presented in Figure A1: the total magnetic energy  $(B_{\rm SB}^2 8\pi)$ , light red in Figure A1(a)); transverse (wrapped) magnetic field energy  $((B_{\rm R}^2 + B_{\rm N}^2)/8\pi)$ , dark red in Figure A1(a). Plotted in Figure A1(b) is the ratio of transverse magnetic field  $B_{\rm R}^2 + B_{\rm N}^2$  divided by the total magnetic field  $B_{\rm SB}^2$  averaged over the R-N cross-section area of the combined FR2-3. FR2 and FR3 are merging (the interval of merging is highlighted in yellow), and that significantly changes their magnetic field structure, leading to a fast decrease of the transverse magnetic field from 0.04–0.02. Thus, merging of FRs leads to fast decay of the transverse (wrapped) components of magnetic field.

## ORCID iDs

O. V. Agapitov https://orcid.org/0000-0001-6427-1596
J. F. Drake https://orcid.org/0000-0002-9150-1841
M. Swisdak https://orcid.org/0000-0002-5435-3544
S. D. Bale https://orcid.org/0000-0002-1989-3596
T. S. Horbury https://orcid.org/0000-0002-7572-4690
J. C. Kasper https://orcid.org/0000-0002-7077-930X
R. J. MacDowall https://orcid.org/0000-0003-3112-4201
F. S. Mozer https://orcid.org/0000-0002-2011-8140
T. D. Phan https://orcid.org/0000-0002-2573-7457
N. E. Raouafi https://orcid.org/0000-0003-2409-3742
M. Velli https://orcid.org/0000-0002-2381-3106

### References

Agapitov, O. V., Wit, T. D., de, Mozer, F. S., et al. 2020, ApJL, 891, L20 Akhavan-Tafti, M., Kasper, J., Huang, J., & Bale, S. 2021, A&A, 650, A4 Bale, S. D., Badman, S. T., Bonnell, J. W., et al. 2019, Natur, 576, 237 Bale, S. D., Goetz, K., Harvey, P. R., et al. 2016, SSRv, 204, 49 Balogh, A., Forsyth, R. J., Lucek, E. A., Horbury, T. S., & Smith, E. J. 1999, GeoRL, 26, 631

```
Bhattacharjee, A., Huang, Y.-M., Yang, H., & Rogers, B. 2009, PhPl, 16,
Biskamp, D. 1986, PhFl, 29, 1520
Borovsky, J. E. 2016, JGRA, 121, 5055
Case, A. W., Kasper, J. C., Stevens, M. L., et al. 2020, ApJS, 246, 43
Cassak, P. A., Shay, M. A., & Drake, J. F. 2009, PhPl, 16, 120702
Chen, Q., Otto, A., & Lee, L. C. 1997, JGRA, 102, 151
Chen, Y., & Hu, Q. 2022, ApJ, 924, 43
Chen, Y., Hu, Q., Zhao, L., et al. 2020, ApJ, 903, 76
Chen, Y., Hu, Q., Zhao, L., Kasper, J. C., & Huang, J. 2021, ApJ, 914, 108
Cowley, S. W. H., & Owen, C. J. 1989, P&SS, 37, 1461
Dahlburg, R. B., Boncinelli, P., & Einaudi, G. 1997, PhPl, 4, 1213
Drake, J. F., Agapitov, O., Swisdak, M., et al. 2021, A&A, 650, A2
Drake, J. F., Swisdak, M., Che, H., & Shay, M. A. 2006, Natur, 443, 553
Dudok de Wit, T., Krasnoselskikh, V. V., Bale, S. D., et al. 2020, ApJS,
  246, 39
Farrell, W. M., MacDowall, R. J., Gruesbeck, J. R., Bale, S. D., & Kasper, J. C.
  2020, ApJS, 249, 28
Fermo, R. L., Drake, J. F., & Swisdak, M. 2010, PhPl, 17, 010702
Fisk, L. A., & Kasper, J. C. 2020, ApJL, 894, L4
Fox, N. J., Velli, M. C., Bale, S. D., et al. 2016, SSRv, 204, 7
Froment, C., Krasnoselskikh, V., de Wit, T. D., et al. 2021, A&A, 650, A5
Gosling, J. T., & Phan, T. D. 2013, ApJL, 763, L39
He, J., Zhu, X., Yang, L., et al. 2020, arXiv:2009.09254
Horbury, T. S., Matteini, L., & Stansby, D. 2018, MNRAS, 478, 1980
Horbury, T. S., Woolley, T., Laker, R., et al. 2020, ApJS, 246, 45
Jannet, G., Wit, T. D., Krasnoselskikh, V., et al. 2021, JGRA, 126, e28543
Kahler, S. W., Crocker, N. U., & Gosling, J. T. 1996, JGRA, 101, 24373
Kasper, J. C., Abiad, R., Austin, G., et al. 2016, SSRv, 204, 131
Kasper, J. C., Bale, S. D., Belcher, J. W., et al. 2019, Natur, 576, 228
Krasnoselskikh, V., Larosa, A., Agapitov, O., et al. 2020, ApJ, 893, 93
Laker, R., Horbury, T. S., Bale, S. D., et al. 2021, A&A, 650, A1
Landi, S., Hellinger, P., & Velli, M. 2006, GeoRL, 33, L14101
Larosa, A., Krasnoselskikh, V., Wit, T. D., de Agapitov, O., & Froment, C.
  2021, A&A, 650, A3
Lee, L. C., & Fu, Z. F. 1985, GeoRL, 12, 105
Macneil, A. R., Owens, M. J., Wicks, R. T., & Lockwood, M. 2020, MNRAS,
  498, 5273
Malaspina, D. M., Ergun, R. E., Bolton, M., et al. 2016, JGRA, 121, 5088
Martinović, M. M., Klein, K. G., Kasper, J. C., et al. 2020, ApJS, 246, 30
Moldwin, M. B., Ford, S., Lepping, R., Slavin, J., & Szabo, A. 2000, GeoRL,
Mozer, F. S., Agapitov, O. V., Bale, S. D., et al. 2020, ApJS, 246, 68
Mozer, F. S., Bale, S., Bonnell, J., et al. 2021, ApJ, 919, 60
Neugebauer, M., & Goldstein, B. E. 2013, in SOLAR WIND 13, AIP Conf.
  Proc. 1539 (Melville, NY: AIP), 46
Odstrcil, D., Vandas, M., Pizzo, V. J., & MacNeice, P. 2003, in SOLAR WIND
  TEN: AIP Conf. Proc. 679 (Melville, NY: AIP), 699
Oka, M., Phan, T. D., Krucker, S., Fujimoto, M., & Shinohara, I. 2010, ApJ,
  714, 915
Phan, T. D., Bale, S. D., Eastwood, J. P., et al. 2020, ApJS, 246, 34
```

Phan, T. D., Gosling, J. T., Paschmann, G., et al. 2010, ApJL, 719, L199

```
Phan, T. D., Paschmann, G., Gosling, J. T., et al. 2013, GeoRL, 40, 11 Pritchett, P. L. 2008, JGRA, 113, A6
Ruffolo, D., Matthaeus, W. H., Chhiber, R., et al. 2020, ApJ, 902, 94
Russell, C. T., & Elphic, R. C. 1978, SSRv, 22, 681
Schwadron, N. A., & McComas, D. J. 2021, ApJ, 909, 95
Shoda, M., Chandran, B. D. G., & Cranmer, S. R. 2021, ApJ, 915, 52
Slavin, J. A., Lepping, R. P., Gjerloev, J., et al. 2003, JGRA, 108, 10
Song, H. Q., Chen, Y., Li, G., & Kong, X. L. 2012, PhRvX, 2, 021015
Sterling, A. C., & Moore, R. L. 2020, ApJL, 896, L18
Swisdak, M., Opher, M., Drake, J. F., & Bibi, F. A. 2010, ApJ, 710, 1769
Tenerani, A., Velli, M., Matteini, L., et al. 2020, ApJS, 246, 32
```

```
Whittlesey, P. L., Larson, D. E., Kasper, J. C., et al. 2020, ApJS, 246, 74
Woodham, L. D., Horbury, T. S., Matteini, L., et al. 2021, A&A, 650, L1
Yamauchi, Y., Suess, S. T., Steinberg, J. T., & Sakurai, T. 2004, JGRA, 109, A03104
Zank, G. P., Nakanotani, M., Zhao, L.-L., Adhikari, L., & Kasper, J. 2020, ApJ, 903, 1
Zeiler, A., Biskamp, D., Drake, J. F., et al. 2002, JGRA, 107, 1230
Zhao, L.-L., Zank, G. P., Adhikari, L., et al. 2020, ApJS, 246, 26
Zhou, M., Berchem, J., Walker, R. J., et al. 2017, PhRvL, 119, 055101
Zhou, M., Pang, Y., Deng, X., Huang, S., & Lai, X. 2014, JGRA, 119, 6177
```